

Solar Wind Energy Input: The Primary Control Factor of Magnetotail Reconnection Site

Tsugunobu Nagai¹ and Iku Shinohara²

¹No.

²The Institute of Space and Astronautical Science, JAXA.

Corresponding author: Tsugunobu Nagai (nagai@stp.isas.jaxa.jp)

Key Points:

- The strong solar wind energy input produces favorable conditions for an onset of magnetic reconnection in the postmidnight sector of the plasma sheet
- The medium and weak solar wind energy input forms favorable conditions for the onset of magnetic reconnection in earlier magnetic local times
- Duskside preference of the tail dynamics is caused by the solar wind conditions at the Earth distance.

Abstract

In this paper, we examine the solar wind energy input (expressed by $-V_x \times B_s$, where V_x is the x component of the solar wind velocity and B_s is the southward component of the interplanetary magnetic field IMF B_z) for an onset of magnetic reconnection in the near-Earth magnetotail. There are 41 events in which in situ observations of magnetic reconnection were made by Geotail. Magnetic reconnection in the postmidnight (premidnight) sector of the plasma sheet occurred under strong (weak) solar wind energy input conditions. Furthermore, we study temporal variations in the solar wind energy input with two different approaches using ground magnetic field observations and proton injections at geosynchronous altitude. These two analyses confirmed the preference of the postmidnight sector for the onset of magnetic reconnection under the strong solar wind energy input conditions. It is also found that the medium and weak solar wind energy input moves the onset location to earlier magnetic local times. The onset location of magnetic reconnection in the near-Earth magnetotail is controlled by the solar wind energy input through the global magnetospheric dynamics during the loading period.

1 Introduction

Magnetic reconnection occurs in the near-Earth magnetotail in association with the onset of magnetospheric substorms. It converts magnetic energy that is previously stored in the magnetotail to plasma kinetic and thermal energy and produces various dynamic phenomena in the magnetosphere-ionosphere system. It produces fast plasma flows, which are observed more frequently in the premidnight (dusk) sector of the plasma sheet relative to those in the postmidnight (dawn) sector (e.g., Nagai et al., 1998). Satellite observations reveal that the occurrence of auroral brightening is high in the 21–24 magnetic local time (MLT) range (e.g., Liou et al., 2001; Frey et al., 2004). Hence, the tail fast plasma flow results are consistent with the occurrence of auroral brightening corresponding to an onset of substorms.

Nagai & Shinohara (2021) reported distribution of in situ magnetic reconnection observations in the near-Earth magnetotail (at radial distances of 20–30 R_E) in association with substorm onsets made by Geotail over the period of 1994–2019. Magnetic reconnection can be observed in the 21–02 MLT (corresponding to the region of $Y_{GSM} = +15$ to $-10 R_E$). The important finding of their study is that magnetic reconnection has a short dawn-dusk X-line corresponding to 1-h MLT. There are several examples of magnetic reconnection in the postmidnight sector of the plasma sheet, and they are mostly observed in highly active geomagnetic conditions and storms by Geotail (Nagai et al., 2013,

2015). The Cluster mission observed the ion diffusion region in magnetic reconnection near $Y_{\text{GSM}} = -5 R_E$ (Eastwood et al., 2010), and the postmidnight event on August 21, 2002 was observed during a storm. During an intense storm on May 28, 2017, the Magnetospheric Multiscale mission made in situ observations of the ion diffusion region at ($X_{\text{GSM}} = -19.3 R_E$, $Y_{\text{GSM}} = -11.8 R_E$, $Z_{\text{GSM}} = 0.78 R_E$) (Rogers et al., 2019). Hence, magnetic reconnection can be formed in the postmidnight sector of the plasma sheet. It may be conceivable that magnetic reconnection observed in the postmidnight sector is a dawnward extension of the X-line initially formed in the premidnight sector. However, magnetic reconnection in the postmidnight sector produces a substorm current system in the same sector. Any dawnward or duskward extension of the X-line is not confirmed (Nagai & Shinohara, 2021).

It is reasonable to attribute an onset of magnetic reconnection to pre-conditions in the plasma sheet during the loading period (the growth phase of substorms). In the growth phase of a substorm, magnetic field lines are transported to the magnetotail as the loading process, and the magnetic field intensity increases in the tail lobes (e.g., Caan et al., 1975, Shukhtina et al., 2014). The plasma sheet thinning is a well-known characteristic of the growth phase (e.g., Baumjohann et al., 1991, 1992). It is accompanied by an increase in the total pressure of the plasma sheet, which is mainly caused by an increase in the plasma density (e.g., Nagai et al., 1997). However, it is not simply caused by any pressure balance effect (e.g., Sergeev et al., 2011, Saito et al., 2011, Yushkov et al., 2021), and plasma transport processes should operate (e.g., Hsieh & Otto, 2015). Since it is difficult to sample many plasma flows during the pure growth phase (not affected by previous substorm activities) by spacecraft in the plasma sheet, the plasma flow pattern producing the dynamics during the growth phase is not well explored.

It is anticipated that the plasma flow pattern in the magnetotail changes with the state of the solar wind. Indeed, Nagai et al. (2005) showed that the solar wind energy input is the most influential factor that determines the radial distance of magnetic reconnection in the magnetotail. Here, the solar wind energy input is expressed by $-V_x \times B_s$, where V_x is the x component of the solar wind velocity and B_s is the southward component of the interplanetary magnetic field IMF B_z . This value, which is expressed as VBs in this study, is similar to that of the solar wind electric field; however, it can more effectively express the energy input from the solar wind to the magnetosphere through dayside magnetic reconnection. We examined various solar wind parameters during the magnetic reconnection events studied by Nagai & Shinohara (2021). The solar wind energy input manifests the

most prominent characteristics for magnetic reconnection in the postmidnight sector.

In this paper, we study temporal variations of the solar wind energy input in three different ways to examine its impact on the onset location of magnetic reconnection in the magnetotail. First, we investigate temporal variations of the solar wind energy input for 41 magnetic reconnection events observed in the magnetotail by Geotail. Unfortunately, this sample number is considered small. Nagai & Shinohara (2021) discovered that each magnetic reconnection forms a substorm current system and that its center is located just west of the magnetic reconnection site. The center of the substorm current system can be used as a proxy for the meridian of the magnetic reconnection site. Second, we examine 414+211 positive bays observed at mid-latitude ground magnetic field stations. Nagai & Shinohara (2021) also discovered that a sharp dipolarization in the magnetic field with proton injections occurs at geosynchronous altitude ($6.6 R_E$) in the meridian of the magnetic reconnection site. Finally, we examine 371 proton injections at geosynchronous altitude. The results of these three different investigations show that the strong solar wind energy input produces favorable conditions for the onset of magnetic reconnection in the postmidnight sector. It is also found that the continuous medium and weak solar wind energy input moves the onset location to earlier MLTs.

The remainder of this paper is categorized as follows: Section 2 describes the data sets used in this study. Section 3 describes the main analyses. Section 4 discusses the significance of the present results for the magnetotail dynamics. Section 5 gives the conclusions.

2 Data

The Geotail spacecraft was used to conduct magnetic field and plasma observations in the plasma sheet for the period of 1998–2020. All magnetic reconnection events used in this study are the same as those selected by Nagai & Shinohara (2021). Any magnetic reconnection event that met the selection criteria by Nagai & Shinohara (2021) was not obtained in 2020. Magnetic field data were obtained through the magnetic field experiment MGF (Kokubun et al., 1994), and ion and electron data were obtained through the low-energy plasma experiment LEP (Mukai et al., 1994).

Ground magnetic field data consist of 1-s (from Japanese and US stations) and 1-min (from other stations) digital data. This study presents magnetic field data

using H (northward) and D (eastward) components. Even when digital data are presented as X- and Y-component data, they are used as H- and D-component data. The data used in this study were obtained from mid- and low-latitude stations; therefore, there is no significant discrepancy between these two coordinate systems. The station name and ABB (abbreviation) code were used according to the World Data Center for Geomagnetism, Kyoto, Data Catalog, No. 32. Information about the geographic and geomagnetic locations of the ground stations is shown in the Data Catalog. The geomagnetic indices AU and AL (from Kyoto University before 2014 and from SuperMAG after 2015) were used.

We also used data obtained by GOES-13 at 75° W, GOES-14 at 105° W, and GOES-15 at 135° W (through November 2018) and 128° W (after December 2018). Magnetic field data in the VDH coordinate system were used. In this system, H (northward) is antiparallel to the Earth's dipole axis, D (azimuthal east) is orthogonal to H and a radius vector to the satellite, and V (nearly radial outward) completes the Cartesian coordinate system. Therefore, the directions of the H and D components are the same as those used for ground magnetic field data. The Energetic Particle Sensor MAGnetospheric Proton Detector and Energetic Particle Sensor MAGnetospheric Electron Detector provided proton (>80 keV) and electron (>30 keV) fluxes, respectively, in five channels. More detailed information is available in Nagai et al. (2019). Energetic electron (>200 keV) fluxes observed by the geosynchronous meteorological spacecraft Himawari-8 (140° E) were also used to monitor electron injections and particle trapping boundary motion (Walker et al., 1976) to identify substorm onsets.

The solar wind data were obtained by the spacecraft ACE. The OMNI 1-min data were used to examine any changes in the solar wind dynamic pressure and to exclude any possible ambiguity in the solar wind traveling time from the L1 point to the Earth. We also examined the Wind and Geotail data when necessary..

3 Analyses of the solar wind energy input for magnetic reconnection

3.1 Geotail in situ magnetic reconnection observations

Nagai & Shinohara (2021) examined 56 magnetic reconnection events in the near-Earth magnetotail (at radial distances of 20–30 R_E) observed by Geotail in 1994–2019. Here, 41 of those events were used in which ACE solar wind observations were available. Figure 1 shows the distribution of the Geotail footpoint locations in MLT. This distribution is not different from that using the original 56 events (Nagai & Shinohara, 2021) and that using 71 events (Nagai et

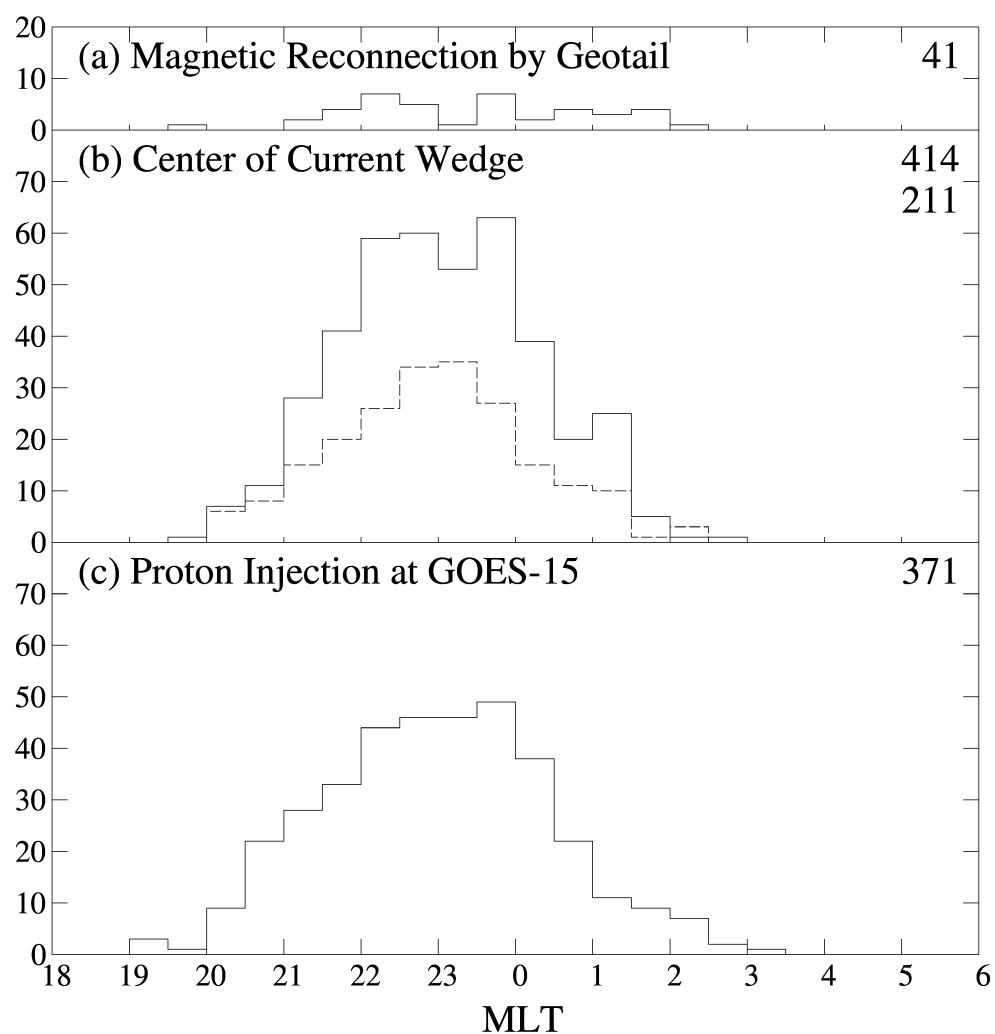
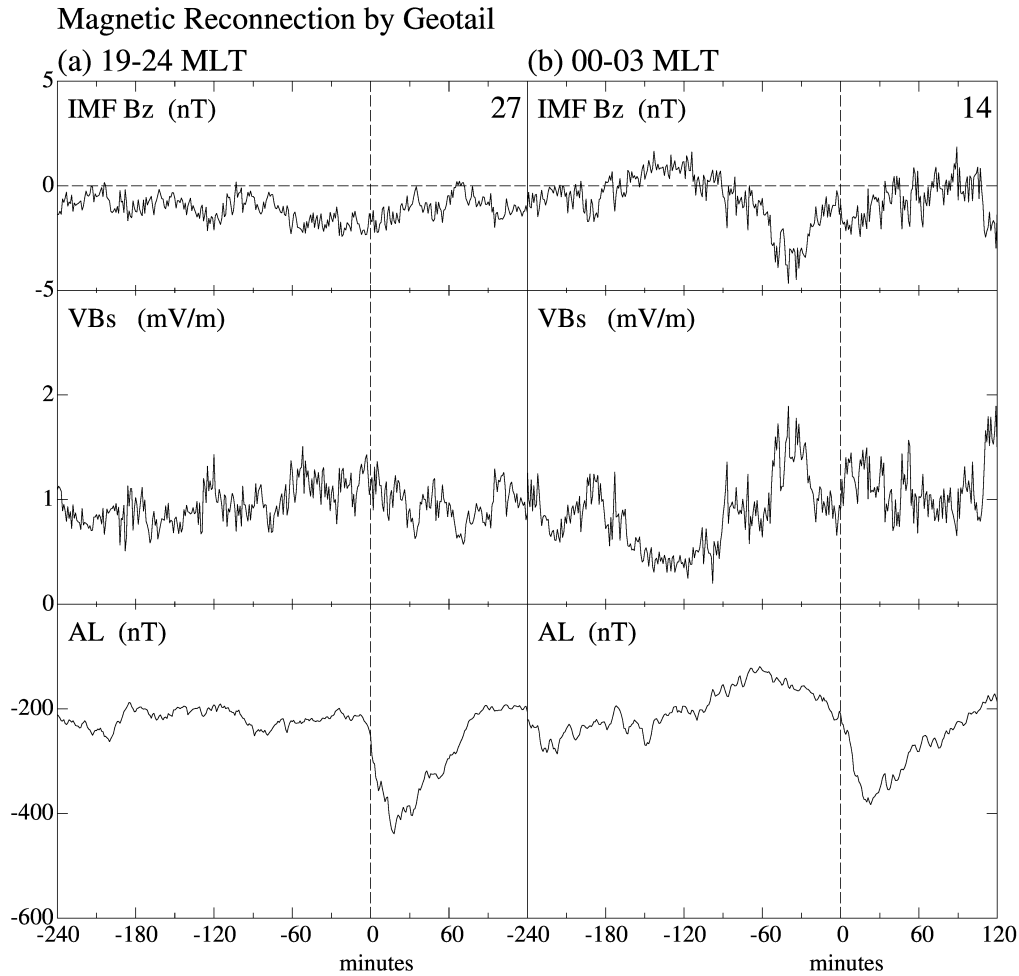


Figure 1. (a) MLT distribution of 41 magnetic reconnection events observed by Geotail. (b) MLT distributions of 414 positive bays in 2015–2019 and 211 positive bays in 2020–2021 (dashed line). (c) MLT distribution of 371 proton injection events observed by GOES-15.

183



184

185

186

187

188

189

Figure 2. Average IMF Bz, solar wind energy input VBs, and auroral electrojet index AL variations for Geotail magnetic reconnection events for the period from -240 min to $+120$ min for 27 events in the 19–24 MLT range (a), and for 14 events in the 00–03 MLT range (b).

al., 2015). The plasma sheet in the near-Earth magnetotail of $Y_{\text{GSM}} = +10$ to $-10 R_E$ are almost equally sampled so that the distribution can represent the occurrence frequency of magnetic reconnection. Although magnetic reconnection is observed with high occurrence in the premidnight sector, there are events in the postmidnight sector.

Here, solar wind conditions were examined for two MLT groups: the events in the premidnight sector (27 events) and those in the postmidnight sector (14 events). Figure 2 shows the average variations of IMF Bz, solar wind energy input VBs (expressed by $-V_x \times B_s$, where V_x is the x component of the solar wind velocity and B_s is the southward component of the interplanetary magnetic field Bz), and auroral electrojet index AL. The zero epoch is the time when Geotail detected tailward plasma flows leading to electron heating (the most essential indication of magnetic reconnection). The AL index results show that the zero epoch well corresponds to an onset of substorms. Although there are no significant differences in the magnitudes of substorms in AL, clear differences exist in the solar wind conditions before the substorm onset. The solar wind energy input VBs is strong prior to the onset of magnetic reconnection occurring in the postmidnight sector. IMF Bz is continuously southward in the time from -240 min for magnetic reconnection occurring in the premidnight sector. Since the number of magnetic reconnection events is small, these two findings will be further examined using the two different approaches.

3.2 Location of the substorm current wedge

McPherron et al. (1973) proposed a substorm current wedge, which can be used to model a substorm current system. A substorm current wedge is composed of downward (into the ionosphere) field-aligned currents in the eastern part and upward (from the ionosphere) field-aligned currents in the western part. These field-aligned currents produce a positive bay signature in the northward component, H, of the magnetic field at mid- and low-latitudes on the ground. Furthermore, they cause changes in the east-west component, D, of the magnetic field at mid-latitudes on the ground and in the vicinity of the geosynchronous altitude in space. The eastern downward field-aligned currents produce negative D variations (the western deflection), whereas the western upward field-aligned currents produce positive D variations (the eastward deflection) in the Northern Hemisphere. The D sign is the opposite in the Southern Hemisphere. Based on the analyses by Nagai & Shinohara (2021), the zero D deflection meridian is used as the center of the substorm current system in this study.

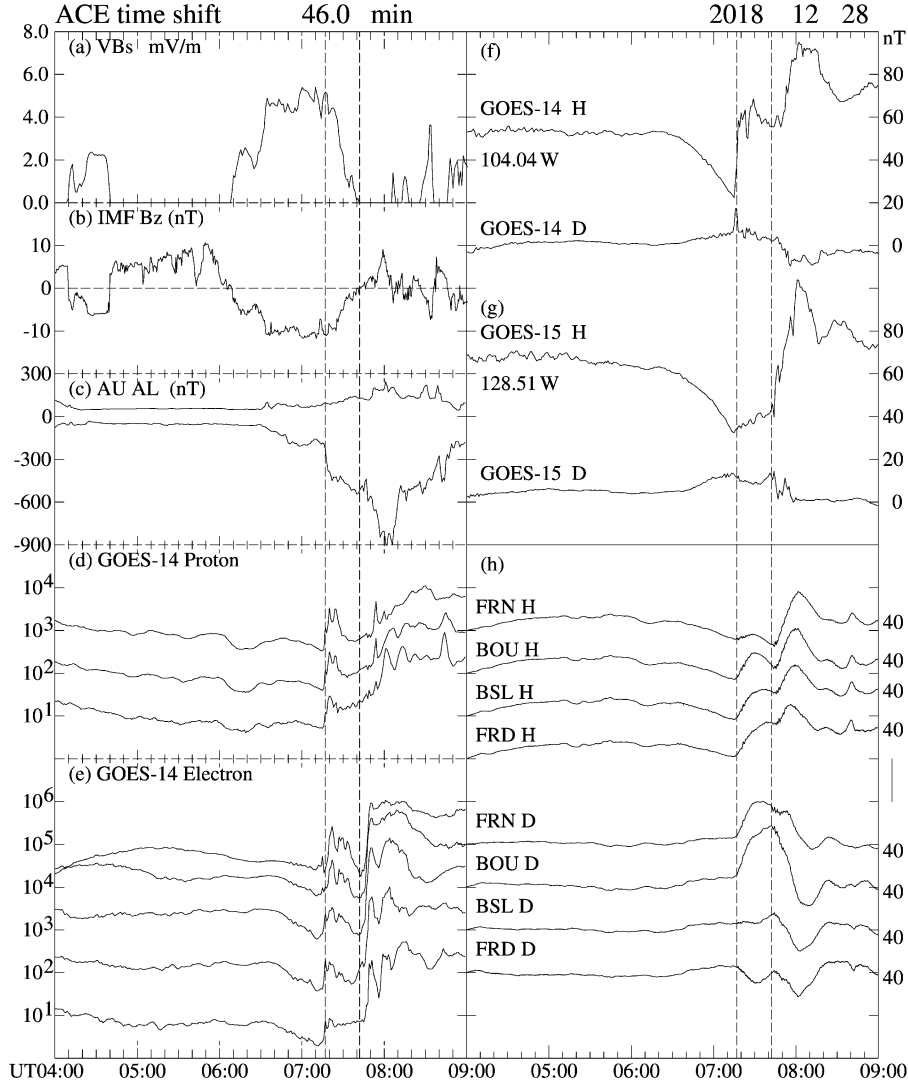


Figure 3. The solar wind energy input VBs, IMF Bz, and Super MAG auroral electrojet indices AU and AL, 80–110, 110–170, and 170–250 keV proton fluxes and 30–50, 50–100, 100–200, 200–350, and 350–600 keV electron fluxes at GOES-14 for the period of 04:00–09:00 UT on December 28, 2018. The unit of the fluxes is $\text{cm}^{-2} \text{s}^{-1} \text{sr}^{-1} \text{keV}^{-1}$. The magnetic field (H and D) is at GOES-14 and GOES-15, and ground magnetic field data (H and D components) are from Fresno (FRN), Boulder (BOU) Stennis (BSL), and Fredericksburg (FRD). The vertical line on the right side corresponds to 40 nT for ground magnetic field data. Vertical dashed lines show 07:17 UT and 07:42 UT onset times.

Figure 3 presents a clear-cut event that was observed on December 28, 2018. This event demonstrates that the center of the substorm current system can form in the postmidnight sector, even for a well-isolated substorm, after the absolutely quiet period, not during storms. IMF Bz maintained its northward direction within the period from 04:40 UT to 06:09 UT (time-shifted) and the auroral electrojet activity subsided. At 06:10 UT, IMF Bz became southward, and the solar wind energy input VBs exceeded more than 4.0 mV/m for one hour. There were two successive onsets at 07:17 UT and 07:42 UT (vertical dashed lines in Figure 3). For the first onset, GOES-14 near 00:30 MLT detected a sharp dipolarization with a positive D spike in the magnetic field (Figure 3f) and proton injections (Figure 3d). For the second onset, GOES-15 near 23:18 MLT detected a sharp dipolarization (Figure 3g) (no proton and electron data were available). Figure 3h shows the ground magnetic field observations from four U.S. stations Fresno (FRN), Boulder (BOU), Stennis (BSL), and Fredericksburg (FRD). A positive H bay started at 07:17 UT and another started at 07:42 UT. For the first onset, the D deflection was almost zero at Stennis (BSL) near 01:20 MLT, whereas for the second onset the zero D meridian was located west of Fresno near 23:30 MLT. For the second onset, a positive D deflection is seen at Honolulu near 21:07 MLT. At the first onset, a sharp negative bay caused by the westward electrojet started at Fort Churchill (00:33 MLT), and at the second onset, another sharp negative bay started at Fort Simpson (22:40 MLT) in the auroral zone (not shown here). These westward electrojet activities produced a two-step decrease in the AL index. The ground magnetic observations are fairly consistent with the duskward shift of the sharp dipolarization region at geosynchronous altitude. In this substorm activity, the first onset occurred in the postmidnight sector, while the second onset position shifted duskward. The first onset in the postmidnight sector evolved into a medium-sized substorm, and it was not any pseudo-onset. This event suggests that it is important to consider the temporal development of substorm activity.

It is not easy to obtain many substorm onsets without any selection biases. Furthermore, good coverage of ground magnetic field observations is needed to determine the center of the substorm current system. We collected well-separated dipolarization events in the magnetic field at geosynchronous altitude using the GOES-13, GOES-14, and GOES-15 data in the period from January 2015 to December 2019, in which at least two spacecraft made observations at 2-h or 4-h separated longitudes. This procedure mainly covers events in the 03:00–09:00 UT range, corresponding to the US nighttime. The ground stations FRN, BOU, BSL, and FRD were used for most cases. Then, we identify a positive bay and its zero D deflection meridian according to the method adopted by Nagai & Shinohara

(2021). Therefore, we use well-isolated events, and we take the first onset when there are successive onsets. Considering the December 28, 2018 event (Figure 3), the first onset at 07:17 UT is taken, but the second onset at 07:42 UT is not selected. It is difficult to use events in highly active conditions (storm activities) and the period when the solar wind dynamic pressure changes significantly, since H and D variations are fairly irregular. These limitations are inevitable when the ground magnetic field data are used. We can identify the onset meridian for 414 events. Out of these 414 events, 320 events (77%) were obtained in the time period of 05–09 UT. The MLT distribution of these events is presented in Figure 1. The center of the substorm current wedge forms mostly in the 22–24 MLT range, and there are 91 events (22.0 %) in the postmidnight sector. The characteristics seen in the MLT distribution are very similar to those in the occurrence of the auroral brightening (e.g., Frey et al., 2004). For example, 82.9 % of the events are distributed in the 21.0–24.5 MLT range and the median is 23.0 MLT. Hence, the procedure adopted here samples reasonably representative events.

Figure 4 presents the average variations of IMF Bz, solar wind energy input VBs, and auroral electrojet index AL for four MLT groups: 88 events in 19–22 MLT, 119 events in 22–23 MLT, 116 events in 23–24 MLT, and 91 events in 00–04 MLT. The AL index results show that the zero epoch well corresponds to an onset of substorms. The next three characteristics emerge.

1. The strong solar energy input before the onset is seen for the postmidnight sector.
2. The solar wind energy input before the onset becomes weaker in earlier MLTs.
3. The IMF Bz is continuously southward in earlier MLTs, resulting in continuous substorm activities.

We also collected energetic flux recovery events using the Himawari-8 data to obtain a positive bay. The high-energy electron flux data can be used to identify an onset of the well-isolated substorm even in other UT ranges (Nagai, 1982). We identified the onset meridian for 211 events in 2020–2021. The MLT distribution of these events is presented in Figure 1. Out of 211 events, 139 events (66%) were obtained in the time period of 08–13 UT, and the ground magnetic stations Honolulu (HON), Eyrewell (EYR), Canberra (CNB), Memambetsu (MMB), and Kakioka (KAK) were used for most cases. Figure 5 shows the average variations of IMF Bz, solar wind energy input VBs, and auroral electrojet index AL presented in the same format used in Figure 4. There are 49 events in 20–22 MLT, 60 events in 22–23 MLT, 62 events in 23–24 MLT, and 40 events in 00–03 MLT. The three characteristics obtained in the previous analysis can be found in the results using the totally different data set.

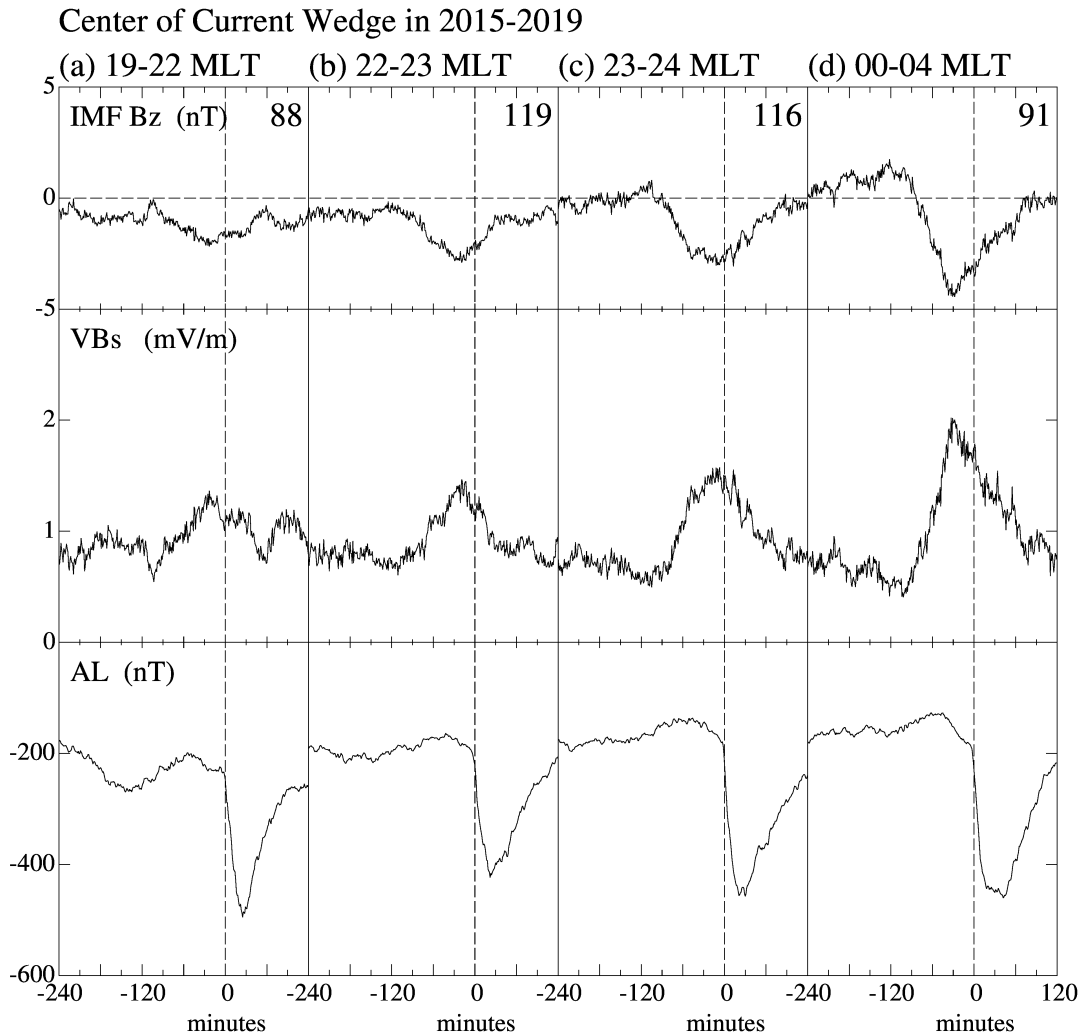


Figure 4. Average IMF Bz, solar wind energy input VBs, and auroral electrojet index AL variations for four MLT groups of mid-latitude positive bay events for the period from -240 min to $+120$ min for the data set in 2015–2019.

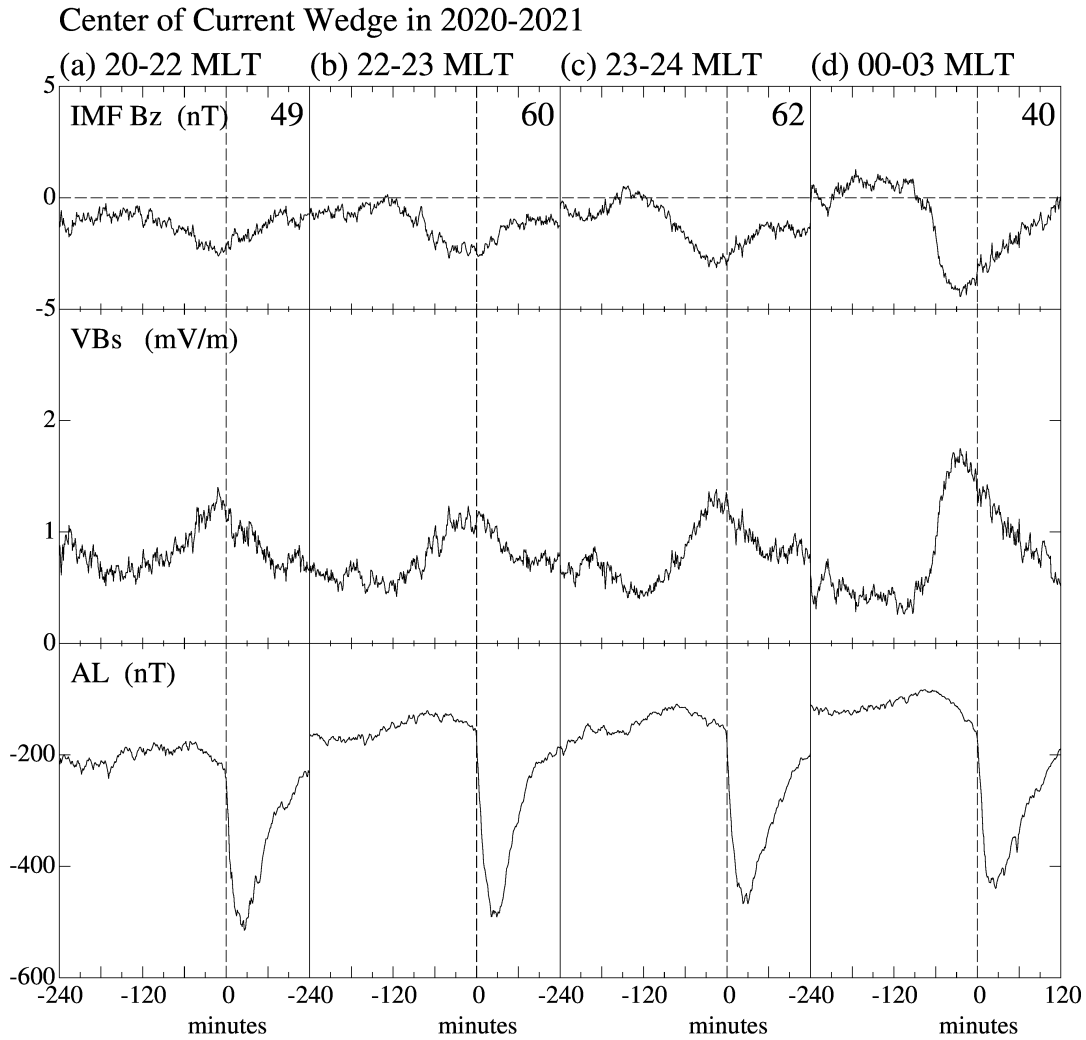


Figure 5. Average IMF Bz, solar wind energy input VBs, and auroral electrojet index AL variations for four MLT groups of mid-latitude positive bay events for the period from -240 min to +120 min for the data set in 2020–2021.

3.3 Location of proton injections

Proton (>80 keV) injections are observed with a sharp dipolarization in the magnetic field with a positive D deflection indicating the upward field-aligned currents (Nagai et al., 2019). GOES-15 was located at 5° geomagnetic latitude at geosynchronous altitude and can minimize flux changes due to the particle trapping boundary motion (Walker et al., 1976). Furthermore, the proton observations by GOES-15 were nearly continuous over the period from January 2015 to February 2020. We collect proton injection events by GOES-15 according to the method used by Nagai et al. (2019). However, when proton injections were observed earlier by GOES-14 (2-h later MLT) or GOES-13 (4-h later MLT), the proton flux-increase events at GOES-15 were discarded because they were events far from the injection meridian. Several proton flux-increase events are associated with a depression in the total magnetic field. Such events were discarded since they are caused by drifting protons (e.g., Nagai, 1982). We identified 371 proton injection events. Proton injection can be identified even under highly active conditions. Figure 6 shows the average variations in proton flux, electron flux, and magnetic fields. The average variations are fairly consistent with the results presented by Nagai et al. (2019). Figure 1 shows the MLT distribution of the proton injection events. Half of the proton injections occur in the 22–24 MLT range (185 events). There are 90 events in the postmidnight sector and 96 events in the earlier MLT region (19–22 MLT).

Figure 7 presents the average variations of IMF Bz, solar wind energy input VBs, and auroral electrojet index AL for four MLT ranges. The AL index results show that the zero epoch well corresponds to an onset of substorms. IMF Bz is continuously southward in all four MLT ranges. This implies that the proton injections can be selected even during highly active conditions, and the analysis using the proton injection can complement the analysis using the ground magnetic field data. The most important finding is that the results obtained using the proton injection events have the three characteristics highlighted in Section 3.2. A strong solar wind energy input is seen in the 00–04 MLT group. The solar wind energy input becomes weaker in earlier MLTs, and the prolonged southward IMF Bz period becomes prominent in earlier MLTs.

4. The role of the solar wind energy input

The three analyses presented in Section 3 demonstrate that the strong solar wind energy input provides favorable conditions for the onset of magnetic

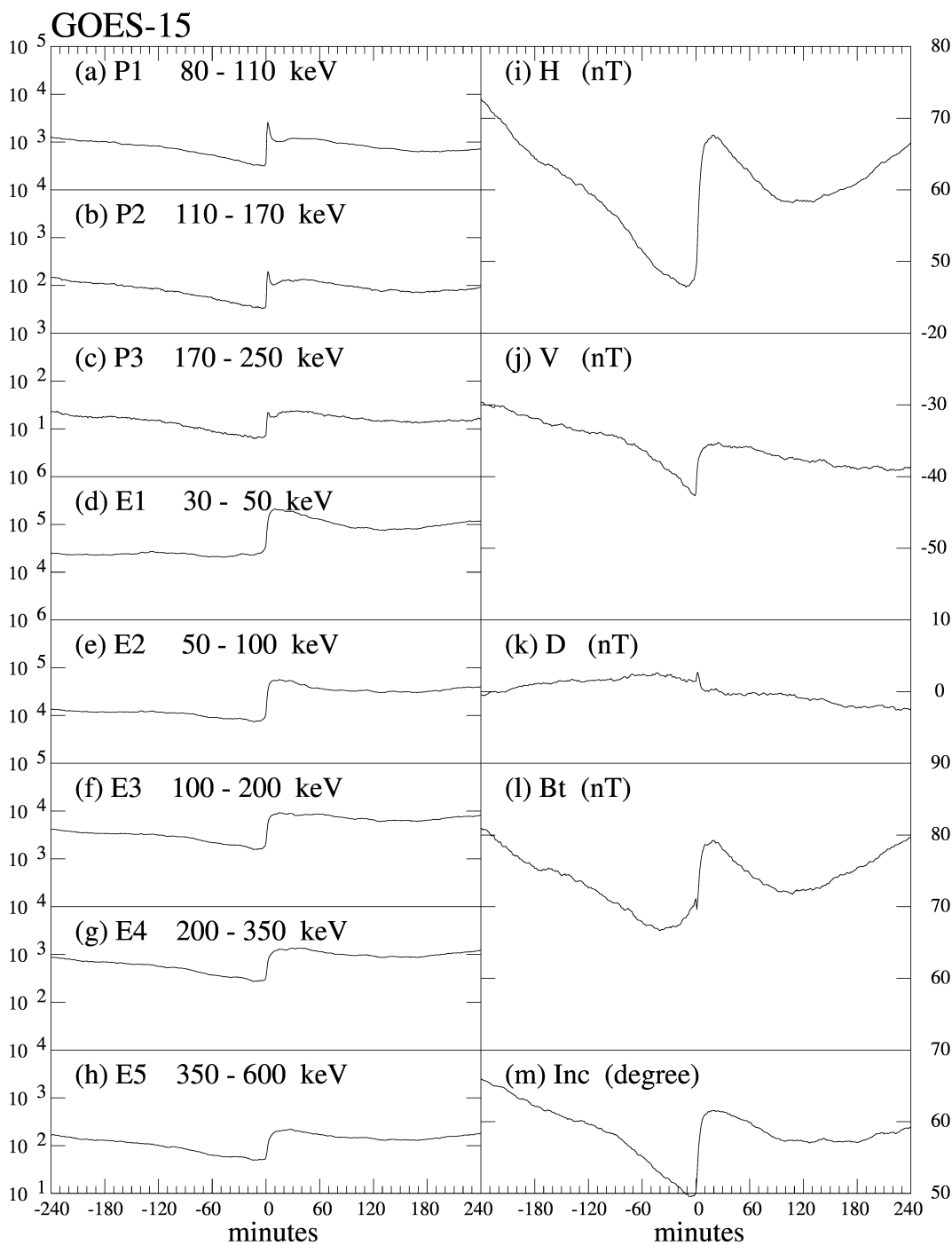


Figure 6. Average proton flux, electron flux, and magnetic field variations derived from 371 proton injection events observed by GOES-15 for the period from -240 min to $+240$ min. The unit of the fluxes is $\text{cm}^{-2} \text{s}^{-1} \text{sr}^{-1} \text{keV}^{-1}$.

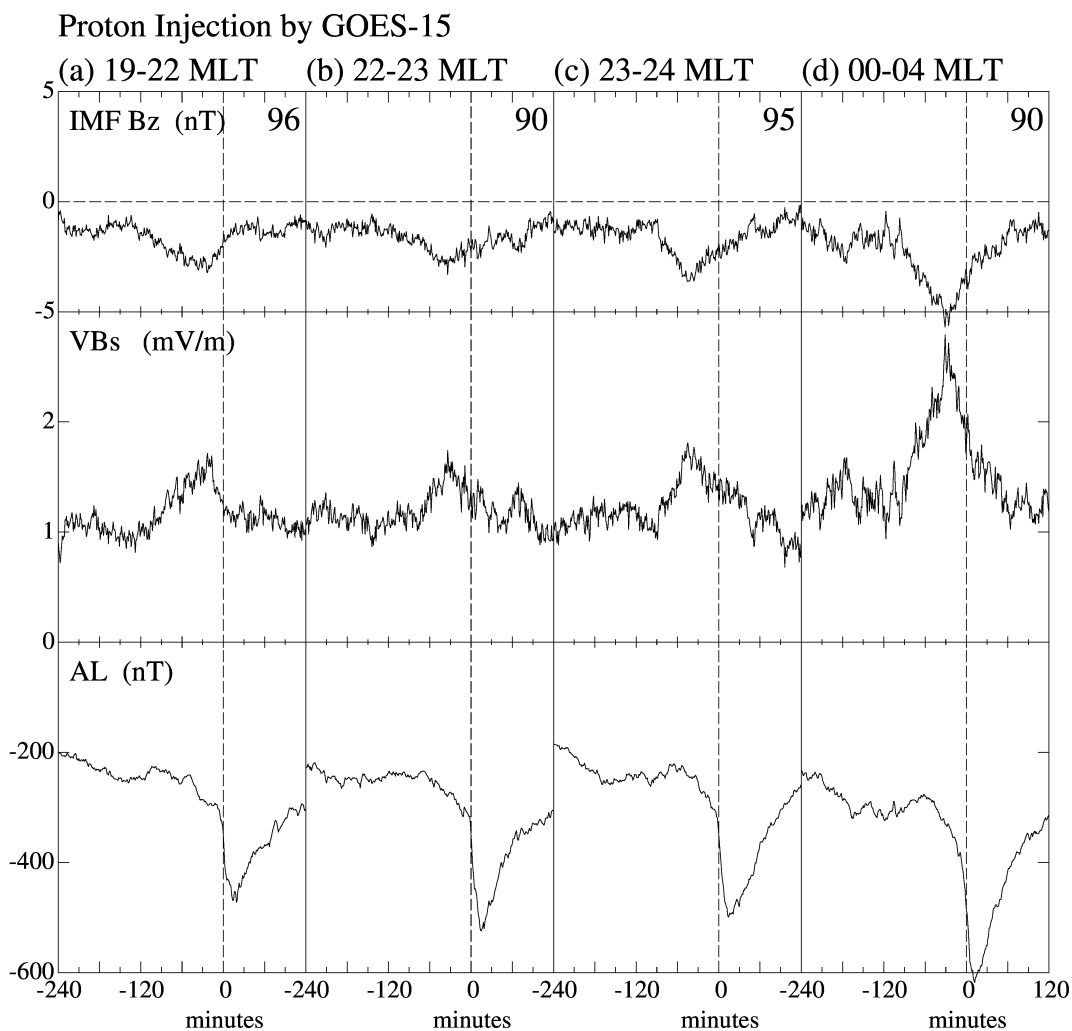


Figure 7. Average IMF Bz, solar wind energy input VBs, and auroral electrojet index AL variations for four MLT groups of proton injection events observed by GOES-15 for the period from -240 min to $+120$ min.

reconnection in the postmidnight sector. However, it is still unknown whether or not there exists any threshold of the total amount of the solar wind energy input leading to an onset of magnetic reconnection. Nagai et al. (2005) examined magnetic reconnection events near the midnight meridian, and they showed that magnetic reconnection forms close to (far from) the Earth in the magnetotail for strong (weak) solar wind energy input conditions. Magnetic reconnection can start even with a small amount of solar wind energy input. Indeed, when the substorm magnitude is determined by the AL index magnitude, both small and large substorms can be recorded. It is expected that an onset of magnetic reconnection forms in the region where the current sheet in the plasma sheet becomes extremely thin. The current sheet thinning is likely controlled by the plasma convection in the near-Earth magnetotail. Under strong solar wind energy input conditions, the plasma convection probably transports plasmas away from the midnight meridian immediately. Under weak solar wind energy input conditions, the plasma convection tends to operate more effectively in the premidnight sector and makes favorable conditions there. The IMF Bz is continuously southward for the events in the 19–22 MT range (Figures 4 and 5).

To test these findings, we conducted analyses for the well-isolated substorm events. We selected 131 events (out of the 414 positive bay events) in which any previous substorm activities are not discernible in the AL index for the 3-h period before the onset. This selection rule can sample the events similar to the December 28, 2018 event (Figure 3). Figure 8 presents the results of the analyses for isolated events and all events. With this procedure, the AL index becomes small before the onset (the magnitude of AL is less than 100 nT). The IMF Bz becomes northward, and the solar wind energy input becomes small for the events in the 00–04 MLT range for the period of –240 min to –60 min. We envisage that magnetic reconnection occurs in the postmidnight sector during storms and during highly active conditions. This phenomenon is true. However, storm activity is not a necessary condition for an onset of magnetic reconnection in the postmidnight sector. The strong solar wind energy input leads to an onset of magnetic reconnection in the postmidnight sector even after the quiet period. The results of the analyses for the isolated events also show that in earlier MLTs, the duration of the southward IMF Bz becomes longer, while the magnitude of the northward IMF Bz becomes smaller, indicating that the weak convection produces the thinning in the premidnight sector of the plasma sheet.

It is interesting to note the numbers of the events. In the 23–04 MLT range, 42.5 % of the events are adopted for the isolated events (43 out of 116 in the 23–24 MLT range and 45 out of 91 in the 00–04 MLT range). However, only 12.5 % and

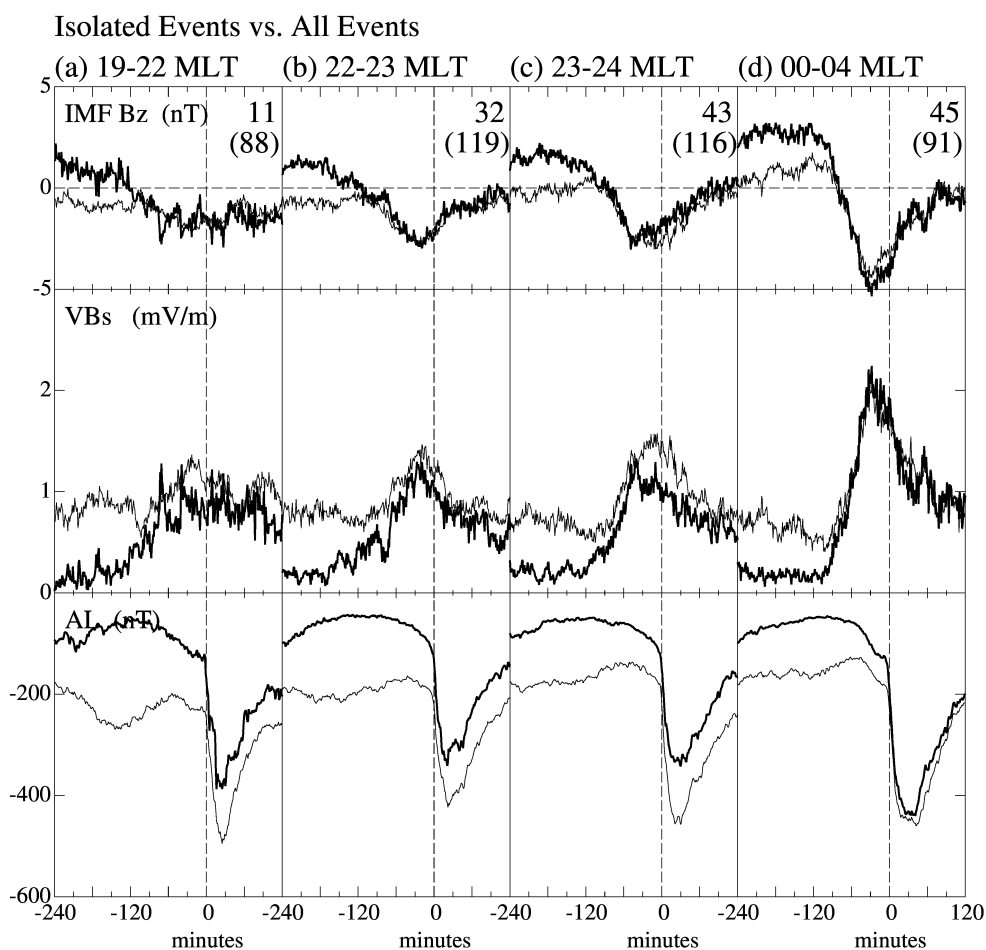


Figure 8. Average IMF Bz, solar wind energy input VBs, and auroral electrojet index AL variations for four MLT groups of well-isolated mid-latitude positive bay events (thick curves) for the period from -240 min to $+120$ min. The results from all events (shown in Figure 4) are also presented with thin curves for comparison. The event number is given in the upper right corner of each panel (the number in parenthesis is the event number for all events).

26.9 % are selected for the isolated events in the 19–23 MLT range (11 out of 88 in the 19–22 MLT and 32 out of 119 in the 23–23 MLT). This result indicates that when there is enough solar wind energy input, the favorable condition for the onset of magnetic reconnection can be formed near the midnight meridian. However, when the solar wind energy input is relatively weak, the onset of magnetic reconnection is delayed and the magnetic convection produces the favorable conditions for the onset of magnetic reconnection in earlier MLTs. Hence, the observed high occurrence frequency of magnetic reconnection in the premidnight sector is most likely caused by the fact that the medium solar wind energy input is more common in the solar wind near the Earth than close to the sun.

It is also interesting to compare the IMF Bz temporal variations for the isolated event (thick curves of Figure 8) and those for all events (thin curves of Figure 8). The IMF Bz variations for the period of –90 min to 0 min are almost similar for each MLT sector, although the event numbers are quite different. This indicates that the time history of the solar wind energy input contributes to form the favorable conditions for the onset of magnetic reconnection in the plasma sheet. There are ambiguities in the solar wind and substorm parameters used in the analyses. The solar wind observations at L1 may not correctly represent the solar wind conditions for the solar wind-magnetosphere interaction in some cases. The separation between EYR and CNB is approximately 2-h in the geomagnetic longitude and the separation between CNB and MMB is approximately 1-h. It is not simple to determine the center of the current system precisely. Hence, we should take into account the limitations of the present analyses. In the present stage, we cannot deduce any single parameter (for example, the sum of the solar wind energy input for the 1-h period before the onset) for predicting the onset location.

There might be other factors for determining the MLT location of an onset of magnetic reconnection. The auroral break-up position moves to earlier MLTs in the Northern Hemisphere and to later MLTs in the Southern Hemisphere for IMF $B_y > 0$ (e.g., Liou et al., 2001, Wang et al., 2007, Liou & Newell, 2010, Milan et al., 2010). However, the magnitude of the shift is less than one hour. The influence of the IMF B_y is asymmetric in the northern and southern tail lobes (e.g., Ohma et al., 2019). Thus, it is unlikely that the IMF B_y controls any onset conditions occurring in the equatorial plane (see also Elhawary et al., 2022). The observed shift in the auroral break-up position due to IMF B_y is probably caused by the field line mapping.

Substorm activities intrude into earlier MLTs (the evening sector) during continuous activities (e.g., Wiens & Rostoker, 1975, Iijima & Potemra, 1978). Hence, the ionospheric convection pattern has skewness, which is coupled to convection flows in the magnetotail. Vasyliunas (1970), in his pioneering work, proposed that the skewness is attributed to the high ionospheric conductivity of the auroral oval. Yasuhara et al. (1983) and Barbosa (1984) presented conceptual models, and Lotko et al. (2014) implemented a more sophisticated ionosphere-magnetosphere global simulation. These studies demonstrated that the rotation of the convection system increases as the Hall conductivity increases. In this mechanism, the ionosphere controls the magnetotail convection through the ionosphere-magnetosphere coupling. This mechanism might work in medium and weak continuous activities. However, this mechanism cannot produce the onset of magnetic reconnection in the postmidnight sector, especially during storms. Furthermore, the onset location of magnetic reconnection can shift dawnward in the premidnight sector during the continuously high activity. In the double-onset substorm event on September 16, 2017, studied by Nagai & Shinohara (2021), the first onset occurred near the 22:00 MLT meridian at 04:32 UT, while the second onset occurred near 24:00 MLT at 05:05 UT. Geotail made in situ observations of magnetic reconnection only for the second onset. Hence, there was the dawnward jump of the magnetic reconnection site in the two successive onsets. There are other examples for the dawnward jump of the onset meridian in Geotail observations, which will be investigated in a separate paper. Hence, the magnetosphere-ionosphere coupling might change the magnetotail convection pattern; however, it cannot become the most effective.

Lu et al. (2018) suggested that the duskward preference of magnetic reconnection is of the plasma sheet origin. The Hall electric field can be induced when the plasma sheet is thinning. The Hall electric field (toward the neutral sheet) may transport field lines with plasmas dawnward, resulting in the further thinning of the duskside plasma sheet. However, in this mechanism the thinning process can be hampered in the dawnside plasma sheet. Hence, this possibility contradicts the dawnward jump of the magnetic reconnection site and the magnetic reconnection occurring in the postmidnight sector during storms.

This paper demonstrates that the strong solar wind energy input makes the favorable conditions for the onset of magnetic reconnection in the postmidnight sector. Sun et al. (2016) reported the dawnward preference of fast plasma flows in the Mercury magnetotail, which is opposite to the duskward preference in the near-Earth magnetotail. In Mercury, the solar wind energy input can always be strong

due to its closeness to the sun, so the finding in this study would explain the Mercury situation.

5 Conclusions

This study examined the behavior of the solar wind energy input (expressed by $-V_x \times B_s$) for magnetic reconnection in the near-Earth magnetotail in association with an onset of magnetospheric substorms. The in situ observations of magnetic reconnection in the magnetotail were not sufficient yet in the present stage. It is difficult to deduce the precise locations of magnetic reconnection in the magnetotail for comprehensive statistical studies. The event number (41 events) from the Geotail observations was not enough; however, there is the prominent characteristic that magnetic reconnection can form in the postmidnight sector of the plasma sheet in the strong solar wind energy input conditions. Two different analyses were conducted using the ground magnetic field observations and the proton injections at geosynchronous altitude. The preference of the postmidnight sector for the onset of magnetic reconnection during the strong solar wind energy input was confirmed. Furthermore, it was found that the medium and weaker solar wind energy input moves the onset location to earlier MLTs. Onset conditions of magnetic reconnection are likely regulated with the global dynamics of the magnetosphere. This study provides a clue to further understanding of preconditions for the onset of magnetic reconnection in the near-Earth magnetotail.

Acknowledgments

The work at ISAS/JAXA was supported by MEXT/JSPS KAKENHI Grant 17H06140.

Data Availability Statement

The data sets used in this study are publicly available. All Geotail data are from the Data Archives and Transmission System (DARTS) of the Institute of Space and Astronautical Science (ISAS) (<http://www.darts.isas.jaxa.jp>) and they are easily obtained. The authors calculated the Geotail footprint using <https://sscweb.gsfc.nasa.gov/cgi-bin/Locator.cgi>. The GOES data are obtained from NOAA National Centers for Environmental Information (<http://www.ngdc.noaa.gov/stp/satellite/goes/index.html>) and the NASA/CDAWeb

(<http://cdaweb.gsfc.nasa.gov>). The ACE and Wind magnetic field and NASA OMNI data are obtained from the NASA/CDAWeb (<http://cdaweb.gsfc.nasa.gov>). The Himawari-8 energetic electron data are obtained from <https://aer-nc-web.nict.go.jp/himawari-seda/>. The digital ground magnetic field data and geomagnetic indices are provided by the World Data Center for Geomagnetism at Kyoto University (<http://wdc.kugi.kyoto-u.ac.jp/index.html>). Information on the ground magnetic stations can be found in the Data Catalog (pdf) of WDC at Kyoto. Some of the digital magnetic field data are provided by the THEMIS website (<http://themis.ssl.berkeley.edu/index.shtml>) and by Super MAG (<http://supermag.jhuapl.edu/>). Geomagnetic indices are also provided by Super MAG.

References

- Barbosa, D. D. (1984). An energy principle for high-latitude electrodynamics. *Journal of Geophysical Research*, 89(A5), 2881–2890. <https://doi.org/10.1029/JA089iA05p02881>
- Baumjohann W., Paschmann, G., Nagai, T., & Lühr, H. (1991) Superposed epoch analysis of the substorm plasma sheet, *J. Geophys. Res.*, 96(A7), 11605-11608. <https://doi.org/10.1029/91JA00775>
- Baumjohann W., Paschmann, G., & Nagai, T. (1992) Thinning and thickening of the plasma sheet, *J. Geophys. Res.*, 97(A11), 17173-17175. <https://doi.org/10.1029/92JA01519>
- Caan, M. N., McPherron, R. L., & Russell, C. T. (1975). Substorm and interplanetary magnetic field effects on the geomagnetic tail lobes. *Journal of Geophysical Research*, 80, 191–194. <https://doi.org/10.1029/JA080i001p00191>
- Eastwood, J. P., Phan, T. D., Øieroset, M., & Shay, M. A. (2010). Average properties of the magnetic reconnection ion diffusion region in the Earth's magnetotail: The 2001–2005 Cluster observations and comparison with simulations. *Journal of Geophysical Research*, 115, A08215. <https://doi.org/10.1029/2009JA014962>
- Elhawary, R., Laundal, K. M., Reistad, J. P., & Hatch, S. M. (2022). Possible ionospheric influence on substorm onset location. *Geophysical Research Letters*, 49, e2021GL096691. <https://doi.org/10.1029/2021GL096691>

Frey, H. U., Mende, S. B., Angelopoulos, V., & Donovan, E. F. (2004), Substorm onset observations by IMAGE-FUV, *J. Geophys. Res.*, 109, A10304. <https://doi.org/10.1029/2004JA010607>

Hsieh, M.-S., & A. Otto (2015), Thin current sheet formation in response to the loading and the depletion of magnetic flux during the substorm growth phase, *J. Geophys. Res. Space Physics*, 120, 4264–4278. <https://doi.org/10.1002/2014JA020925>

Iijima, T., & Potemra, T. A., (1978) Large-scale characteristics of field-aligned currents associated with substorms, *J. Geophys. Res.*, 83(A2), 599-615. <https://doi.org/10.1029/JA083iA02p00599>

Kokubun, S., Yamamoto, T., Acuña, M. H., Hayashi, K., Shiokawa, K., & Kawano, H. (1994). The Geotail magnetic field experiment. *Journal of Geomagnetism and Geoelectricity*, 46, 7–21. <https://doi.org/10.5636/jgg.46.7>

Liou, K., & Newell, P. T. (2010). On the azimuthal location of auroral breakup: Hemispheric asymmetry. *Geophysical Research Letters*, 37, L23103. <https://doi.org/10.1029/2010GL045537>

Liou, K., Newell, P. T., Sibeck, D. G., Meng, C. -I., Brittnacher, M., & Parks, G. (2001). Observation of IMF and seasonal effects in the location of auroral substorm onset. *Journal of Geophysical Research: Space Physics*, 106, 5799–5810. <https://doi.org/10.1029/2000JA003001>

Lotko, W., Smith, R. H., Zhang, B., Ouellette, J. E., Brambles, O. J., & Lyon, J. G. (2014). Ionospheric control of magnetotail reconnection. *Science*, 345, 184–187. <https://doi.org/10.1126/science.1252907>

Lu, S., Pritchett, P. L., Angelopoulos, V., & Artemyev, A. V. (2018). Formation of dawn-dusk asymmetry in Earth's Magnetotail thin current sheet: A three-dimensional particle-in-cell simulation. *Journal of Geophysical Research: Space Physics*, 123, 2801–2814. <https://doi.org/10.1002/2017JA025095>

McPherron, R. L., Russell, C. T., & Aubry, M. P. (1973). Satellite studies of magnetospheric substorms on August 15, 1968: 9. Phenomenological model for substorms. *Journal of Geophysical Research*, 78, 3131–3149. <https://doi.org/10.1029/JA078i016p03131>

- Milan, S. E., A. Grocott, and B. Hubert (2010), A superposed epoch analysis of auroral evolution during substorms: Local time of onset region, *J. Geophys. Res.*, 115, A00I04. <https://doi.org/10.1029/2010JA015663>
- Mukai, T., Machida, S., Saito, Y., Hirahara, M., Terasawa, T., Kaya, N., Obara, T., Ejiri, M., & Nishida, A. (1994). The Low-Energy Particle (LEP) experiment onboard the Geotail satellite. *Journal of Geomagnetism and Geoelectricity*, 46, 669–692. <https://doi.org/10.5636/jgg.46.669>
- Nagai, T. (1982). Local time dependence of electron flux changes during substorms derived from multi-satellite observations at synchronous orbit. *Journal of Geophysical Research*, 87(A5), 3456–3468. <https://doi.org/10.1029/JA087iA05p03456>
- Nagai, T., & Shinohara, I. (2021). Dawn-dusk confinement of magnetic reconnection site in the near-Earth magnetotail and its implication for dipolarization and substorm current system. *Journal of Geophysical Research: Space Physics*, 126, e2021. <https://doi.org/10.1029/2021JA029691>
- Nagai, T., Mukai, T., Yamamoto, T., Nishida, A., Kokubun, S., & Lepping, R. P. (1997). Plasma sheet pressure changes during the substorm growth phase. *Geophysical Research Letters*, 24, 963–966. <https://doi.org/10.1029/97GL00374>
- Nagai, T., Fujimoto, M., Saito, Y., Machida, S., Terasawa, T., Nakamura, R., Yamamoto, T., Mukai, T., Nishida, A., & Kokubun, S. (1998). Structure and dynamics of magnetic reconnection for substorm onsets with Geotail observations. *Journal of Geophysical Research: Space Physics*, 103(A3), 4419–4440. <https://doi.org/10.1029/97JA02190>
- Nagai, T., Fujimoto, M., Nakamura, R., Baumjohann, W., Ieda, A., Shinohara, I., Machida, S., Saito, Y., & Mukai, T. (2005). Solar wind control of the radial distance of the magnetic reconnection site in the magnetotail, *Journal of Geophysical Research*, 110, A09208. <https://doi.org/10.1029/2005JA011207>
- Nagai, T., Shinohara, I., Zenitani, S., Nakamura, R., Nakamura, T. K. M., Fujimoto, Saito, Y., & Mukai, T. (2013). Three-dimensional structure of magnetic reconnection in the magnetotail from Geotail observations. *Journal of Geophysical Research: Space Physics*, 118, 1667–1678. <https://doi.org/10.1002/jgra.50247>

- 662 Nagai, T., Shinohara, I., & Zenitani, S. (2015). The dawn-dusk length of the X line
663 in the near-Earth magnetotail: Geotail survey in 1994–2014. *Journal of*
664 *Geophysical Research: Space Physics*, 120, 8762–8773.
665 <https://doi.org/10.1002/2015JA021606>
666
- 667 Nagai, T., Shinohara, I., Singer, H. J., Rodriguez, J., & Onsager, T. G. (2019).
668 Proton and electron injection path at geosynchronous altitude. *Journal of*
669 *Geophysical Research: Space Physics*, 124, 4083–4103.
670 <https://doi.org/10.1029/2018JA026281>
671
- 672 Ohma, A., Østgaard, N., Reistad, J. P., Tenfjord, P., Laundal, K. M., Moretto
673 Jørgensen, T., Haaland, S. E., Krcelic, P., & Milan, S. (2019). Observations of
674 asymmetric lobe convection for weak and strong tail activity. *Journal of*
675 *Geophysical Research: Space Physics*, 124, 9999–10017.
676 <https://doi.org/10.1029/2019JA026773>
677
- 678 Rogers, A. J., Farrugia, C. J., & Torbert, R. B. (2019). Numerical algorithm for
679 detecting ion diffusion regions in the geomagnetic tail with applications to MMS
680 tail season 1 May to 30 September 2017. *Journal of Geophysical Research: Space*
681 *Physics*, 124, 6487–6503. <https://doi.org/10.1029/2018JA026429>
682
- 683 Saito, M. H., Fairfield, D., Le, G., Hau, L.-N., Angelopoulos, V., McFadden, J. P.,
684 Auster, U., Bonnell, J. W., & Larson, D. (2011). Structure, force balance, and
685 evolution of incompressible cross-tail current sheet thinning. *Journal of*
686 *Geophysical Research: Space Physics*, 116, A10217.
687 <https://doi.org/10.1029/2011JA016654>
688
- 689 Sergeev, V., Angelopoulos, V., Kubyshkina, M., Donovan, E., Zhou, X.-Z.,
690 Runov, A., Singer, H., McFadden, J., & Nakamura, R. (2011). Substorm growth
691 and expansion onset as observed with ideal ground-spacecraft THEMIS coverage.
692 *Journal of Geophysical Research: Space Physics*, 116, A00I26.
693 <https://doi.org/10.1029/2010JA015689>
694
- 695 Shukhtina, M. A., Dmitrieva, N. P., & Sergeev, V. A. (2014). On the conditions
696 preceding sudden magnetotail magnetic flux unloading. *Geophysical Research*
697 *Letters*, 41, 1093–1099. <https://doi.org/10.1002/2014GL059290>
698
- 699 Sun, W. J., S. Y. Fu, J. A. Slavin, J. M. Raines, Q. G. Zong, G. K. Poh, & T. H.
700 Zurbuchen (2016), Spatial distribution of Mercury’s flux ropes and reconnection

fronts: MESSENGER observations, *J. Geophys. Res. Space Physics*, 121, 7590–7607. <https://doi.org/10.1002/2016JA022787>

Vasyliunas, V. M. (1970). Mathematical models of magnetospheric convection and its coupling to the ionosphere, pp. 60–71, in *Particles and Fields in the Magnetosphere*, Edited by McCormac, B. M. Springer, Dordrecht

Walker, R. J., Erickson, K. N., Swanson, R. L., & Winckler, J. R. (1976). Substorm-associated particle boundary motion at synchronous orbit. *Journal of Geophysical Research*, 81, 5541–5550. <https://doi.org/10.1029/JA081i031p05541>

Wang, H., Lüher, H., Ma, S. Y., & Frey, H. U. (2007). Interhemispheric comparison of average substorm onset locations: Evidence for deviation from conjugacy. *Annales Geophysicae*, 25, 989–999. <http://www.ann-geophys.net/25/989/2007/>

Wiens, R. G., & Rostoker, G. (1975). Characteristics of the development of the westward electrojet during the expansive phase of magnetospheric substorms, *Journal of Geophysical Research*, 80, 2109–2128. <https://doi.org/10.1029/JA080i016p02109>.

Yasuhara, F., Greenwald, R., & Akasofu, S. -I. (1983). On the rotation of the polar cap potential pattern and associated polar phenomena. *Journal of Geophysical Research*, 88(A7), 5773–5777. <https://doi.org/10.1029/JA088iA07p05773>

Yushkov, E. V., Petrukovich, A. A., Artemyev, A. V., & Nakamura, R. (2021). Thermodynamics of the magnetotail current sheet thinning. *Journal of Geophysical Research: Space Physics*, 126, e2020. <https://doi.org/10.1029/2020JA028969>

Figure Captions

Figure 1. (a) MLT distribution of 41 magnetic reconnection events observed by Geotail. (b) MLT distributions of 414 positive bays in 2015–2019 and 211 positive bays in 2020–2021 (dashed line). (c) MLT distribution of 371 proton injection events observed by GOES-15.

Figure 2. Average IMF B_z, solar wind energy input VBs, and auroral electrojet index AL variations for Geotail magnetic reconnection events for the period from –240 min to +120 min for 27 events in the 19–24 MLT range (a), and for 14 events in the 00–03 MLT range (b).

Figure 3. The solar wind energy input VBs, IMF Bz, and Super MAG auroral electrojet indices AU and AL, 80–110, 110–170, and 170–250 keV proton fluxes and 30–50, 50–100, 100–200, 200–350, and 350–600 keV electron fluxes at GOES-14 for the period of 04:00–09:00 UT on December 28, 2018. The unit of the fluxes is $\text{cm}^{-2} \text{s}^{-1} \text{sr}^{-1} \text{keV}^{-1}$. The magnetic field (H and D) is at GOES-14 and GOES-15, and ground magnetic field data (H and D components) are from Fresno (FRN), Boulder (BOU) Stennis (BSL), and Fredericksburg (FRD). The vertical line on the right side corresponds to 40 nT for ground magnetic field data. Vertical dashed lines show 07:17 UT and 07:42 UT onset times.

Figure 4. Average IMF Bz, solar wind energy input VBs, and auroral electrojet index AL variations for four MLT groups of mid-latitude positive bay events for the period from –240 min to +120 min for the data set in 2015–2019.

Figure 5. Average IMF Bz, solar wind energy input VBs, and auroral electrojet index AL variations for four MLT groups of mid-latitude positive bay events for the period from –240 min to +120 min for the data set in 2020–2021.

Figure 6. Average proton flux, electron flux, and magnetic field variations derived from 371 proton injection events observed by GOES-15 for the period from –240 min to +240 min. The unit of the fluxes is $\text{cm}^{-2} \text{s}^{-1} \text{sr}^{-1} \text{keV}^{-1}$.

Figure 7. Average IMF Bz, solar wind energy input VBs, and auroral electrojet index AL variations for four MLT groups of proton injection events observed by GOES-15 for the period from –240 min to +120 min.

Figure 8. Average IMF Bz, solar wind energy input VBs, and auroral electrojet index AL variations for four MLT groups of well-isolated mid-latitude positive bay events (thick curves) for the period from –240 min to +120 min. The results from all events (shown in Figure 4) are also presented with thin curves for comparison. The event number is given in the upper right corner of each panel (the number in parenthesis is the event number for all events).